Formation conditions of aluminum-rich chondrules

Tronche, E.J.; Hewins, R.H.; MacPherson, G.J.

published in
Geochimica et Cosmochimica Acta
2007

DOI (link to publisher)
10.1016/j.gca.2007.03.037

document version
Publisher's PDF, also known as Version of record

Available online at www.sciencedirect.com
ScienceDirect
Geochimica et Cosmochimica Acta 71 (2007) 3361–3381
Geochimica et Cosmochimica Acta
www.elsevier.com/locate/gca

Formation conditions of aluminum-rich chondrules

Elodie J. Tronche [a], Roger H. Hewins [a,b], Glenn J. MacPherson [c,*]

[a] *Laboratoire d'Etudes de la Matière Extraterrestre, MNHN & CNRS-UMS2679, 61 rue Buffon, 75005 Paris, France*
[b] *Department of Geological Sciences, Rutgers University, 610 Taylor Road, Piscataway, NJ 08854, USA*
[c] *Department of Mineral Sciences, MRC NHB-119, National Museum of Natural History, Smithsonian Institution, Washington, DC 20560, USA*

Received 4 May 2006; accepted in revised form 30 March 2007; available online 6 May 2007

Abstract

We have studied the formation conditions of Al-rich chondrules by doing isothermal and dynamic crystallization experiments at one atmosphere on four different chondrule analogue compositions within the pure $CaO–MgO–Al_2O_3–SiO_2$ system. For the dynamic crystallization experiments, we cooled from both liquidus and subliquidus peak temperatures (T_{max}), at cooling rates from 5–1000 °C/h. The starting compositions include two with anorthite and two with forsterite as the dominant liquidus phases, all at or near spinel-saturation. One of each pair evolves towards diopside crystallization, and the others cordierite or enstatite crystallization, giving a total of four completely different crystallization sequences analogous to the four basic varieties of Al-rich chondrule recently proposed. Bulk composition is the main controlling factor, both in terms of mineralogy and texture. The textures of the anorthite-rich compositions are more sensitive to T_{max} than they are to cooling rate, whereas the textures of the forsterite-rich compositions are more sensitive to cooling rate. Comparisons of natural Al-rich chondrules having similar compositions to our synthetic analogues indicate that the natural objects reflect a range of peak heating temperatures, ~1400–1500 °C, and cooling rates of 10–500 °C/h for porphyritic chondrules and possibly higher (1000 °C/h) for barred chondrules. These conditions are consistent with the conditions inferred for ferromagnesian chondrules but differ from those inferred for some calcium–aluminum-rich inclusions.

1. INTRODUCTION

Chondrites contain a record of the earliest events in the solar system. Those meteorites are mainly composed of: chondrules, more or less spherical particles of ferromagnesian silicate composition and which (together with chondrule fragments) can constitute 80% of the rock; iron–nickel metal; calcium- and aluminum-rich inclusions (CAIs), and fine-grained matrix that encloses the other components. Chondrules and CAIs have been extensively studied, but their respective origins and relationship to one another are still only partially understood.

Two main types of chondrules exist: type I, depleted in volatiles and FeO and rich in metal; and type II, which are rich in FeO and volatiles and poor in metal (McSween, 1977; Jones, 1990, 1994). Those two types can each be further subdivided into silica-poor (A; olivine-rich) and silica-rich (B; pyroxene-rich) subtypes. Another, rarer, type of chondrule exists, with a more aluminous composition than ferromagnesian chondrules (Bischoff and Keil, 1983a,b, 1984; Bischoff et al., 1985; Sheng et al., 1991; Krot et al., 2001a,b, 2002; MacPherson and Huss, 2005). Al-rich chondrules are of particular interest because they were the first chondrules in which evidence for extinct ^{26}Al (in the form of excess ^{26}Mg) was found (Russell et al., 1996; Srinivasan et al., 2000; Hsu et al., 2003). They are intermediate in composition between ferromagnesian chondrules and some CAIs (plagioclase-rich, known as Type C) (Krot et al., 2001a,b; Krot and Keil, 2002a,b; Krot et al.,

* Corresponding author.
E-mail address: macphers@si.edu (G.J. MacPherson).

0016-7037/$ - see front matter © 2007 Elsevier Ltd. All rights reserved.
doi:10.1016/j.gca.2007.03.037

2004a,b; MacPherson and Huss, 2005). Thus, understanding the formation conditions and processes of Al-rich chondrules may help establish a petrogenetic link between ferromagnesian chondrules and at least some CAIs.

Aluminous chondrules span a wide composition range (e.g., Bischoff and Keil, 1983a,b, 1984; Bischoff et al., 1985) and therefore exhibit comparably diverse mineral assemblages that can include phases such as spinel, olivine, Ca-rich and Ca-poor pyroxenes, plagioclase, and glass. Textures in aluminous chondrules are equally diverse. MacPherson and Huss (2005) showed that the composition range of Al-rich chondrules is continuous, and that the variety of textures as well as mineral assemblages can be directly related to their bulk major element compositions in the context of complex phase equilibrium relationships. Those authors accordingly defined two main varieties of Al-rich chondrules that largely include the many separate "types" identified in previous work (e.g., Bischoff and Keil, 1983b; Sheng et al., 1991):

1. Al-rich [Oliv] chondrules whose mineralogy is dominated by early crystallizing (liquidus or near-liquidus) olivine.
2. Al-rich [Plag] chondrules whose mineralogy is dominated by early crystallizing plagioclase.

Each of these in turn is subdivided into two groups owing to the effects of a phase equilibrium boundary (a thermal divide; see below) that variously affects the liquid lines of descent of melts depending on which side of the divide their compositions lie. MacPherson and Huss (2005) considered as a separate group a variant of Al-rich chondrule denoted by them as Al-rich [glass] chondrules (the Na-, Al-rich chondrules of Bischoff and Keil, 1983b), and which are calcium-poor and typically contain abundant sodium-rich glass. These have a more complex origin than the other Al-rich chondrules, requiring pre-melting metasomatic alteration in order to explain their compositions. MacPherson and Huss (2005) showed that CAIs, Al-rich chondrules (excluding the glass-rich variety), and ferromagnesian chondrules define a continuous composition trend that suggests that volatility-controlled processes and gas/solid reactions produced their compositions (more properly, those of the precursors).

Chondrules and many CAIs have shapes, textures, mineral and chemical compositions characteristic of solidification from molten or partially molten droplets. Therefore they are amenable to experimental petrologic studies in a laboratory, which can constrain the conditions of their melting and crystallization. Such studies have been done on ferromagnesian chondrule and some CAI compositions to define their formation conditions. Stolper (1982), MacPherson et al. (1984), and Stolper and Paque (1986) showed that type B CAI melting temperatures were subliquidus and probably lower than 1400 °C, and the cooling rates were 0.5–50 °C/h. For ferromagnesian chondrules the maximum temperatures were 1400–1850 °C, superliquidus for barred chondrules and subliquidus for porphyritic ones; cooling rates were 10–1000 °C/h (Blander et al., 1976; Lofgren and Russell, 1986; Lofgren, 1989; Hewins and Radomsky, 1990; Lofgren and Lanier, 1990; Radomsky and Hewins, 1990; Connolly and Hewins, 1991; Lofgren, 1996; Hewins and Connolly, 1996; Hewins et al., 2005). We report here the first dynamic crystallization experiments on four different aluminous chondrule compositions, and also for one type C CAI composition, to constrain their peak temperatures and cooling rates, and to test the MacPherson–Huss model relating highly diverse observed textures and modal mineralogy to the predicted crystallization sequences for specific bulk compositions.

2. EXPERIMENTAL METHODS

2.1. Starting compositions and materials

Five starting compositions were used in our experiments, one representing a Type C CAI and the others representing each of the four fundamentally different varieties of Al-rich chondrules (not including the glass-rich variant) of MacPherson and Huss (2005). The choice of these five compositions becomes clear from consideration of Fig. 1, which shows them plotted relative to experimentally-determined liquidus phase equilibrium relationships within the pure CMAS ($CaO–MgO–Al_2O_3–SiO_2$) system; they are projected from spinel (hence all equilibria shown are spinel-saturated) onto the plane $Al_2O_3–Ca_2SiO_4–Mg_2SiO_4$ (see MacPherson and Huss, 2005, for details of this diagram). The bulk composition fields for Type I ferromagnesian chondrules, Al-rich chondrules, and Type C CAIs also are shown. Note how the range of natural Al-rich chondrule bulk compositions spans two major phase equilibrium boundaries that control the crystallization sequences and textures: the spinel-saturated anorthite–forsterite reaction boundary and a thermal divide defined by the join anorthite–forsterite. The reaction curve divides Al-rich chondrules into those having plagioclase (±spinel) as the liquidus phase and those having olivine (±spinel) as the liquidus phase. The thermal divide in turn separates each of those into ones that evolve toward silica saturation and ones that evolve to silica undersaturation (note that the presence of iron or sodium shifts the positions of these boundaries but not their existence).

Accordingly, the four experimental compositions we used (Table 1) represent each of the four Al-rich chondrule varieties, and are based on the mean of natural chondrule compositions except that they consist only of the major CMAS components. Two are in the anorthite-saturated field, one on each side of the thermal divide (PL1 on the silica-undersaturated side and PL2 on the silica-saturated side), and two are in the forsterite-saturated field (OL1 and OL2, straddling the thermal divide as above). The fifth composition, corresponding to a type C CAI, is similar in composition to Al-rich [Plag] chondrules and to composition PL1. However, note that composition Type C CAI plots on the opposite side (relative to PL1) of a line joining the mineral anorthite and the distributary reaction point where the anorthite–forsterite reaction curve hits the pyroxene field; this is more easily seen in Fig. 2, which is an enlarged detail of part of Fig. 1. The significance is that a melt of Type C CAI composition will not hit the anor-

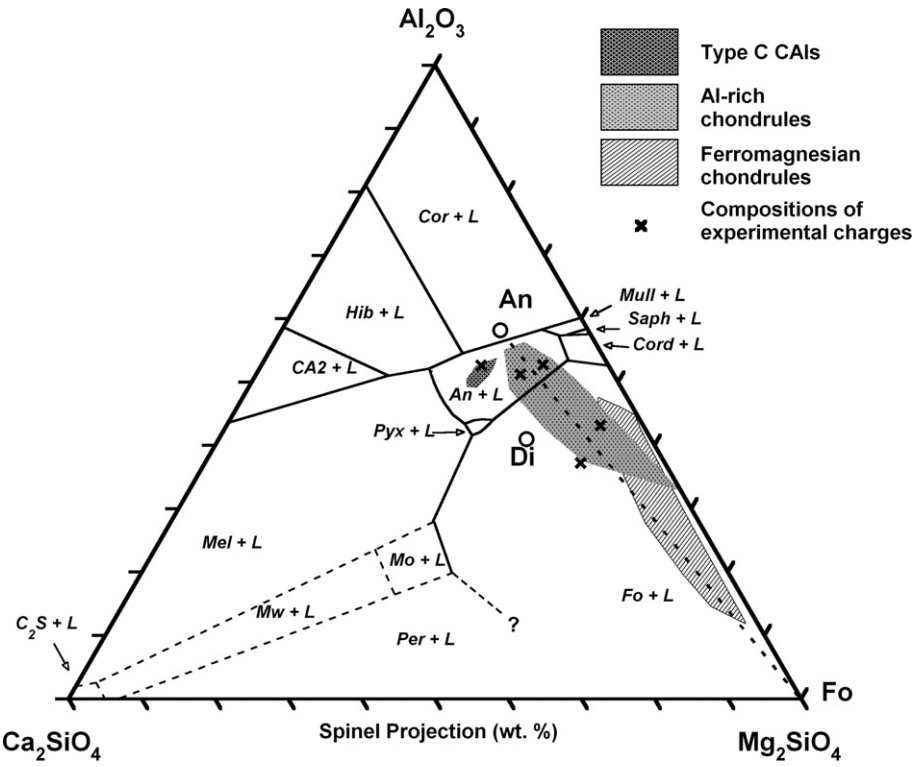

Fig. 1. The five experimental compositions studied in this work (Type C CAI, PL1, PL2, OL1 and OL2) projected from $MgAl_2O_4$ (spinel) onto the plane Ca_2SiO_4–Mg_2SiO_4 (Forsterite)-Al_2O_3 (Corundum). The bulk composition fields for natural Type I ferromagnesian chondrules, Al-rich chondrules and Type C CAIs are shown for comparison, based on data from Jones and Scott (1989), Jones (1994), Wark (1987), Bischoff and Keil (1984), Sheng et al. (1991), and MacPherson and Huss (2005). The field boundaries are spinel-saturated liquidus phase equilibria (see MacPherson and Huss, 2005). Abrreviations: An, anorthite; Cor, corundum; Cord, cordierite; Di, diopside; Fo, forsterite; Gr, Grossite; Hib, hibonite; L, liquid (melt); Mel, melilite solid solution; Mo, monticellite; Mw, merwinite; Mull, mullite; Per, periclase; Pyx, pyroxene solid solution; Saph, sapphirine.

Table 1
Experimental compositions (in wt %) in the CMAS system

	Type C CAI	PL1	PL2	OL1	OL2
SiO_2	37.36	45.26	41.68	41.46	46.92
Al_2O_3	33.94	25.01	31.17	16.55	15.46
MgO	6.35	10.88	14.82	30.04	30.15
CaO	22.35	18.84	12.33	11.95	7.47

thite–forsterite reaction curve and will never crystallize forsterite; a melt of PL1 composition, however, will crystallize forsterite prior to intersecting the pyroxene field.

The five starting materials were made by mixing natural minerals (quartz and corundum) with CaO (made from calcite) and synthetic MgO. Quartz, corundum and calcite were crushed with an automatic tungsten crusher for 1 h each. The calcite powder was converted to CaO by heating to 900 °C for 18 h. MgO was dehydrated for 3 h at 150 °C.

The resulting mixes were crushed by hand in an agate mortar and pressed into pellets using a manual press. These were mounted on Pt wire loops and heated in air in a Del-Tech DT-31-VT-OS muffle tube furnace at 1570 °C. Temperature was controlled by a type S thermocouple ($Pt_{100}/Pt_{90}Rh_{10}$), calibrated to the palladium melting point (1554 °C). Each sample was heated for 50–60 min, and then quenched in water. The resulting charges contain glass but no mineral phases; the main purpose of this first heating is to avoid relict grains from the starting material. Samples were then crushed with ethanol with an agate crusher, to produce five fine powders (grain size 40–63 μm), which constitute the five starting compositions for our experiments. One 35–40 mg pellet of each composition was melted at 1580 °C for 3 h, quenched to glass in water, and analyzed with an electron microprobe in order to accurately determine the bulk composition as given in Table 1.

2.2. Analytical techniques

Polished sections of all runs were studied using a JEOL JSM 840A scanning electron microscope at the Université Paris VI and, also, a FEI Nova NANOSEM 600 field emission scanning electron microscope at the National Museum of Natural History, Smithsonian Institution, in Washington DC. Coarse-grained individual phases were analysed *via* wavelength dispersive spectrometry using a Cameca SX100 electron microprobe at the Université Paris VI, operated at 4 nA beam current and 15 kV, accelerating voltage. In the very finest-grained run products, semi-quantitative (standardless) analyses of phases were obtained using a ThermoNoran System Six energy dispersive X-ray

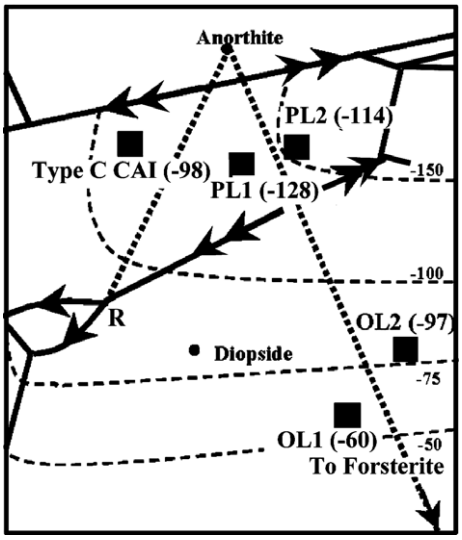

Fig. 2. Detail of Fig. 1, showing the identification of each of the experimental compositions along with their spinel coordinates (in brackets). The dashed lines are contours on the spinel-saturation surface, and comparison of the spinel coordinate for each experimental composition with the value of the spinel-saturation surface at that location indicates whether a composition is spinel saturated or not. For example, composition Type C CAI has a spinel coordinate of −98 and the spinel-saturation surface at that location has a value of ∼−110; therefore composition Type C CAI plots above the surface and is spinel-saturated. The intersection of the anorthite–forsterite tie line (dotted) with the anorthite–forsterite boundary curve marks the position of the thermal divide (opposed arrows). The dotted line connecting anorthite with the anorthite–forsterite–pyroxene (+spinel) distributary reaction point (R) separates bulk compositions within the anorthite primary phase volume (e.g., PL1) that ultimately will crystallize forsterite from those (e.g., Type C CAI) that will not crystallize forsterite.

analytical system attached to the Smithsonian Institution field emission SEM (operated at 12 kV accelerating voltage). All photographs in this manuscript are back-scattered electron (b.s.e.) images.

2.3. Experiments

Isothermal experiments were performed in order to determine the liquidus temperatures, the equilibrium phase assemblages at each temperature, and the phase appearance temperatures. The phase appearance temperature was calculated to be half of the difference between the temperature above its first appearance and the run temperature at which the phase first occurs. For each of the five starting compositions, 10–13 different runs were conducted that differed in their heating temperatures so as to cover the crystallization interval of each bulk composition. In each run, a 30 mg pellet was heated to and held at a fixed temperature for 3.5–18 h and then quenched in water. The details of all isothermal runs are given in Table 2.

Eight to 12 dynamic crystallization experiments were made for each composition, with different heating temperatures and cooling rates. Pellets (25–30 mg) were heated for 2.5–4.5 h, then cooled to 1000 °C at a constant rate and quenched in water. Two starting (maximum) temperatures (T_{max}) were chosen for each composition: near-liquidus and 50–65 °C below the liquidus. For the Type C CAI composition experiments, both starting temperatures were subliquidus: 1396 and 1452 °C. This was done by analogy to Type B CAIs, for which experiments have shown that complete melting did not occur in nature and spinel crystals were present at the time that the natural melts began cooling (see Stolper and Paque, 1986). Cooling rates of 5, 10, 50, 100, 500, 1000 °C/h were chosen for each composition and each T_{max} (except for OL2). The details of all dynamic crystallization runs are given in Table 3.

3. RESULTS

3.1. Isothermal experiments

Fig. 2 shows the contours on the spinel-saturation surface along with the spinel-saturated liquidus phase relationships from Fig. 1; the points for compositions PL1, PL2, OL1, and Type C CAI all plot on or above the spinel-saturation surface and have spinel as the liquidus or near-liquidus phase (their spinel coordinates, in brackets next to each of the compositions, have higher values than the spinel-saturation surface at that location). Composition OL2 plots somewhat below the spinel-saturation surface and forsterite is the liquidus phase; although the phase relationships shown are strictly applicable only to spinel-saturated melts, OL2 is sufficiently close to spinel saturation that inferred equilibria remain valid as will be shown.

The Type C CAI bulk composition lies above the spinel-saturation surface within the anorthite primary phase volume (Figs. 1 and 2); spinel thus is expected to be the liquidus phase, followed at lower temperatures successively by anorthite, melilite and, finally, calcic pyroxene. Our isothermal experiments on this composition yield a liquidus temperature of 1470 ± 12 °C with spinel as the sole phase (Table 2). Anorthite begins to crystallize at 1410 °C. Our experiments went only as low as 1300 °C, and no other phase was observed to crystallize by that temperature. This is consistent with the phase diagram, as melilite and eventually pyroxene are not expected to begin crystallizing until well below 1300 °C (see MacPherson and Huss, 2005, their Fig. 8b); these two phases do occur in the dynamic crystallization experiments. The residual liquid (glass) has a composition close to that of aluminous diopside.

Composition PL1 lies essentially on the spinel-saturation surface within the anorthite primary phase volume (Fig. 2). In this case, spinel and anorthite are expected to approximately co-crystallize at the liquidus and be followed successively by olivine and calcic pyroxene. In the isothermal experiments on this composition, anorthite is the liquidus phase and appears at ∼1401 °C (±8 °C), followed by spinel at 1364 ± 5 °C, forsterite at 1307 ± 7 °C, and diopside at 1270 ± 10 °C. The theoretical vs. experimental discrepancy in the relative crystallization sequence of spinel and anorthite is minor; this bulk composition is so close

Table 2
Isothermal experiments

Composition	Run	Temperature (°C)	Heating time (h)	Phases
CAI	EqCAI#1	1508	14	Gl
	EqCAI#7	1483	3.5	Gl
	EqCAI#2	1458	4	Gl + Sp
	EqCAI#8	1431	15	Gl + Sp
	EqCAI#3	1410	3	Gl + Sp + An
	EqCAI#4	1410	14	Gl + Sp + An
	EqCAI#5	1365	4	Gl + Sp + An
	EqCAI#6	1315	4	Gl + Sp + An
	EqCAI#9	1300	4	Gl + Sp + An
PL1	EqPL1#1	1508	4.1	Gl
	EqPL1#2	1457	4	Gl
	EqPL1#7	1434	3.5	Gl
	EqPL1#3	1410	15.8	Gl
	EqPL1#8	1392	3.6	Gl + An
	EqPL1#4	1370	3.75	Gl + An
	EqPL1#9	1358	15	Gl + An + Sp
	EqPL1#5	1311	3.9	Gl + An + Sp
	EqPL1#10	1300	3.5	Gl + An + Fo + Di
	EqPL1#11	1281	4	Gl + An + Fo + Di
	EqPL1#12	1260	18	Gl + An + Fo + Di
	EqPL1#13	1238	18	An + Fo + Di
	EqPL1#6	1202	46	An + Fo + Di
PL2	EqPL2#1	1502	3.7	Gl
	EqPL2#6	1478	3.9	Gl + Sp
	EqPL2#2	1457	15	Gl + Sp
	EqPL2#3	1410	3.9	Gl + Sp
	EqPL2#7	1392	3.5	Gl + Sp
	EqPL2#4	1368	3.9	Gl + Sp + An
	EqPL2#8	1345	15	Gl + Sp + An
	EqPL2#5	1311	14.7	Gl + Sp + An
	EqPL2#9	1295	3.9	Gl + Sp + An
	EqPL2#10	1275	15	Gl + Sp + An + Fo
	EqPL2#11	1255	4	Gl + An + Fo + Cord
	EqPL2#12	1239	4	Gl + An + Fo + Cord
	EqPL2#13	1210	18	Gl + An + Fo + Cord
OL1	EqOL1#1	1553	10.5	Gl
	EqOL1#2	1478	3.6	Gl + Fo
	EqOL1#3	1435	15	Gl + Fo
	EqOL1#4	1300	3.5	Gl + Fo + An
	EqOL1#5	1279	15	Gl + Fo + An
	EqOL1#6	1250	3.5	Gl + Fo + An + Di
	EqOL1#7	1238	3.5	Gl + Fo + An + Di
	EqOL1#8	1215	15	Gl + Fo + An + Di
OL2	EqOL2#1	1553	5	Gl
	EqOL2#2	1502	3.7	Gl + Fo
	EqOL2#3	1457	3.5	Gl + Fo
	EqOL2#4	1406	18	Gl + Fo
	EqOL2#5	1368	20	Gl + Fo
	EqOL2#6	1311	20	Gl + Fo
	EqOL2#7	1300	10	Gl + Fo
	EqOL2#8	1275	4	Gl + Fo
	EqOL2#9	1255	3	Gl + Fo + An
	EqOL2#10	1241	3.5	Gl + Fo + An + En
	EqOL2#11	1213	3.5	Gl + Fo + An + En

Abbreviations: An, anorthite; Cord, cordierite; Di, Diopside; En, enstatite; Fo, forsterite; Gl, glass; Sp, spinel.

to the spinel-saturation surface that, within uncertainty, it could easily lie somewhat below the saturation surface and have anorthite as the liquidus phase.

Composition PL2 also plots within the anorthite primary phase volume (Fig. 2), but on the opposite side of the thermal divide from PL1 and well above the spinel-sat-

Table 3
Dynamic crystallization experiments

Type C CAI composition	DynCAI#1	DynCAI#2	DynCAI#3	DynCAI#4	DynCAI#5	DynCAI#6	DynCAI#7	DynCAI#8	DynCAI#9	DynCAI#10	DynCAI#11	DynCAI#12
T_{max} (°C)	1452	1396	1452	1396	1452	1396	1452	1396	1452	1396	1452	1396
Time at T_{max} (h)	3	3	3	3	3	3	3	3	2	2	2	2
Cooling rate (°C/h)	5	5	10	10	50	50	100	100	500	500	1000	1000
T_{quench} (°C)	1000	1000	1000	1012	1000	1000	1000	1026	1000	1000	1000	1000
Phases	Sp, An, Al–Di, Mel	Sp, An, Al–Di, Mel	Sp, An, Al–Di, Mel	Sp, An, Al–Di, Mel	Sp, An, Al–Di, Gl	Sp, An, Al–Di, Gl	Sp, An, Al–Di, Gl	Sp, An, Al–Di, Gl	Sp, An, Al–Di, Gl	Sp, An, Al–Di, Gl	Sp, An, Al–Di, Gl	Sp, An, Gl
PL1 composition	DynPL1#1	DynPL1#2	DynPL1#3	DynPL1#4	DynPL1#5	DynPL1#6	DynPL1#7	DynPL1#8	DynPL1#9	DynPL1#10	DynPL1#11	DynPL1#12
T_{max} (°C)	1401	1350	1401	1350	1401	1350	1401	1350	1401	1350	1401	1350
Time at T_{max} (h)	3	3	4	2.5	3	3.5	3	3	2.5	2	1	2.5
Cooling rate (°C/h)	5	5	10	10	50	50	100	100	500	500	1000	1000
T_{quench} (°C)	1049	1011	1000	1000	1000	1000	1000	1000	1000	1000	1000	1000
Phases	Gl, An, Fo, Al–Di	Gl, An, Fo, Al–Di	Gl, An, Fo, Al–Di	Gl, An, Fo, Sp, Al–Di	Gl, An, Fo, Al–Di	Gl, An, Fo, Al–Di	Gl, An, Fo, Al–Di	Gl, An, Fo, Al–Di	Gl, An, Fo, Al–Di	Gl, An, Fo, Al–Di	Gl, An, Fo, Al–Di	Gl, An, Fo, Al–Di
PL2 composition	DynPL2#1	DynPL2#2	DynPL2#3	DynPL2#4	DynPL2#5	DynPL2#6	DynPL2#7	DynPL2#8	DynPL2#9	DynPL2#10	DynPL2#11	DynPL2#12
T_{max} (°C)	1475	1416	1475	1416	1475	1416	1475	1416	1475	1416	1475	1416
Time at T_{max}(h)	3	3	3	2.5	3	3.5	3	3	2.5	2	1	2.5
Cooling rate (°C/h)	5	5	10	10	50	50	100	100	500	500	1000	1000
T_{quench} (°C)	1097	1050	1000	1000	1000	1000	1000	1000	1000	1000	1000	1000
Phases	Gl, An, Sp, Al–En, Fo	Gl, An, Sp, Al–En, Fo	Gl, An, Sp, Al–En, Fo	Gl, An, Sp, Al–En, Fo	Gl, An, Sp, Al–En, Fo	Gl, An, Sp, Al–En, Fo	Gl, An, Sp, Al–En, Fo	Gl, An, Sp, Al–En, Fo	Gl, An, Sp, Al–En, Fo	Gl, An, Sp, Al–En, Fo	An, Sp, mesostasis	Gl, An, Sp, Al–En, Fo
OL1 composition	DynOL1#1	DynOL1#2	—	DynOL1#4	DynOL1#5	DynOL1#6	DynOL1#7	DynOL1#8	DynOL1#9	DynOL1#10	DynOL1#11	DynOL1#12
T_{max} (°C)	1470	1416	—	1416	1470	1416	1470	1416	1470	1416	1470	1416
Time at T_{max} (h)	3	3	—	3	3	3	3	3	3	3	3	3
Cooling rate (°C/h)	5	5	—	10	50	50	100	100	500	500	1000	1000
T_{quench} (°C)	946	916	—	1000	1000	1000	1000	1012	1000	1000	1000	1000
Phases	Fo, Sp, An, Al–Di	Fo, Sp, An, Al–Di	—	Fo, Sp, An, Al–Di	Gl, Fo, Sp, An, Al–Di	Gl, Fo, Sp, An, Al–Di	Gl, Fo, Sp, An, Al–Di	Gl, Fo, Sp, An, Al–Di	Gl, Fo, Sp, An, Al–Di	Gl, Fo, Sp, An, Al–Di	Gl, Fo, Sp, An, Al–Di	Gl, Fo, Sp, An, Al–Di
OL2 composition	DynOL2#1	—	DynOL2#3	DynOL2#4	—	—	—	DynOL2#8	DynOL2#9	DynOL2#10	DynOL2#11	DynOL2#12
T_{max} (°C)	1502	—	1502	1450	—	—	—	1450	1502	1450	1502	1450
Time at T_{max} (h)	3	—	3	1.5	—	—	—	3	3	3	3	3
Cooling rate (°C/h)	5	—	10	10	—	—	—	100	500	500	1000	1000
T_{quench} (°C)	1000	—	50	1000	—	—	—	1000	1000	1000	1000	1000
Phases	Gl, Fo, Sp, An, Al–En	—	Gl, Fo, Sp, An, Al–En	Gl, Fo, Sp, An, Al–En	—	—	—	Gl, Fo, Sp, An, Al–En	Gl, Fo, Sp, An, Al–En	Gl, Fo, Sp, An, Al–En	Mesostasis (Gl), Fo, Sp	Mesostasis (Gl), Fo, Sp

Abbreviations as in Table 2 except: Al–Di, aluminous diopside; Al–En, aluminous enstatite; Mel, melilite solid solution.

uration surface. The expected crystallization sequence is spinel followed successively by anorthite, olivine, and cordierite as the solidus phase. Our isothermal experiments follow this sequence exactly: spinel crystallizes first at a liquidus temperature of approximately 1478 °C. Anorthite appears at 1379 ± 11 °C, forsterite at 1285 ± 10 °C, and finally cordierite crystallizes at ~1255 °C.

Composition OL1 plots within the olivine primary phase volume and lies very close to the spinel-saturation surface. The expected crystallization sequence is forsterite + spinel nearly co-crystallizing at the liquidus, followed by anorthite and, finally, calcic pyroxene. The observed experimental liquidus phase is forsterite, appearing at ~1480 °C. Anorthite crystallizes at 1306 ± 5 °C, followed by diopside at 1250 °C. Charges quenched at temperatures lower than 1250 °C are very fine grained and it is uncertain whether any reached the solidus. None of the equilibrium experiments for this composition contain spinel, contrary to expectations, yet all of the dynamic crystallization runs for this composition do contain spinel. This difference is actually a predictable result of the different ways in which equilibrium vs. dynamic crystallization experiments are conducted. It is mainly evident for compositions in which there is a phase (in this case, spinel) that goes into reaction relationship during the crystallization interval. In the CMAS system, spinel cannot co-crystallize simultaneously with forsterite and anorthite; for any bulk composition in which early-formed spinel and one of the other two phases initially co-crystallize, spinel goes into reaction relationship with the melt once the third phase appears. The discrepancies between isothermal vs. dynamic crystallization experiments arise because isothermal experiments are conducted by bringing the starting material (in this case, quenched glass) up to some specified temperature and holding it there; if that temperature is either below the reaction temperature of spinel with melt + forsterite + anorthite, or above the spinel liquidus, spinel will never appear in the run products because it was never present. Dynamic crystallization experiments, however, begin by complete or nearly-complete melting of the starting material and then proceed by continuous cooling through the entire crystallization interval. Early-formed spinel can be preserved below the reaction temperature if spinel grains become trapped within other phases and hence protected against reaction. For composition OL1, forsterite is the sole crystallizing phase down to at least 1435 °C, and anorthite begins crystallizing no lower than 1300 °C. Spinel presumably crystallizes somewhere in the intervening temperatures but, because no equilibrium experiments were conducted at those intermediate temperatures, it is not observed in our runs.

Composition OL2 also plots within the olivine primary phase volume but on the opposite side of the thermal divide from OL1; OL2 lies below the spinel-saturation surface. The expected crystallization sequence (based on Figs. 1 and 2) is forsterite at the liquidus, followed by spinel, anorthite and finally cordierite. Because this composition is forsterite-saturated rather than spinel saturated, as noted above, another useful diagram is shown in Fig. 3 (from Sheng, 1992), illustrating the phase equilibrium relationships projected from forsterite onto the plane tridymite-diopside-spinel. This diagram confirms the inference from Fig. 2 that spinel will be the second-crystallizing phase after forsterite and that it in turn is followed by anorthite and, finally, cordierite. Spinel is in continuous reaction relationship with the liquid once anorthite joins the crystallizing assemblage; when cordierite also begins to crystallize, if all of the spinel either reacts away or else becomes isolated from further contact from the liquid, the remaining melt proceeds toward silica saturation and enstatite crystallization as indicated on Fig. 3 (Figs. 1 and 2 no longer apply). As in the case of OL1, the equilibrium experimental runs for OL2 are apparently at variance with these expectations in that spinel is not observed even though it is present in all of the dynamic crystallization experiments; the explanation is precisely the same as given above for OL1.

3.2. Dynamic crystallization experiments

3.2.1. Type C CAI composition

All runs for this composition starting at $T_{max} = 1396$ °C have ophitic textures, dominated by euhedral anorthite blades enclosed by calcic pyroxene (Fig. 4). Spinel grains are euhedral, small, and sparse. Melilite is the last phase to crystallize, and is more abundant at faster cooling rates. There is little perceptible effect of cooling rate on grain size, grain shape or texture.

All runs starting at $T_{max} = 1452$ °C (Fig. 4) also have ophitic textures regardless of cooling rate. However, runs at this starting temperature have fewer and larger crystals than the runs at $T_{max} = 1396$ °C with comparable cooling rates. The aspect ratios of plagioclase laths are noticeably higher (more elongate) at faster cooling rates, a feature that is not obvious for the runs at $T_{max} = 1396$ °C.

For this composition, therefore, T_{max} exerts more control on texture than cooling rate. The principal effect of T_{max} is on grain size, with crystals being fewer and larger in the experiments performed at $T_{max} = 1452$ °C than they are at $T_{max} = 1396$ °C, presumably because of more extensive (though still incomplete) destruction of nuclei. Cooling rate has little effect on texture for a given peak temperature.

3.2.2. PL1 composition

All charges have ophitic textures, dominated by anorthite laths enclosed by calcic pyroxene (Fig. 5). Forsterite grains and aluminous glass are interstitial. Spinel grains do occur in these experiments but are rare, owing to the reaction relationship with the liquid once forsterite began to co-crystallize with anorthite. As expected from the phase diagram in Figs. 1 and 2, the chief mineralogical difference between PL1 and Type C CAI is the presence of forsterite and absence of melilite in PL1.

As is the case for Type C CAI runs, T_{max} plays the dominant role in controlling textures for PL1 (Fig. 5). Runs starting at $T_{max} = 1401$ °C ($\sim T_{liquidus}$) are generally coarser grained, have fewer crystal nuclei, and have more elongate anorthite blades than runs started at $T_{max} = 1350$ °C (subliquidus). The main effect of cooling rate, regardless of T_{max}, is on the aspect ratios of the anorthite crystals: they

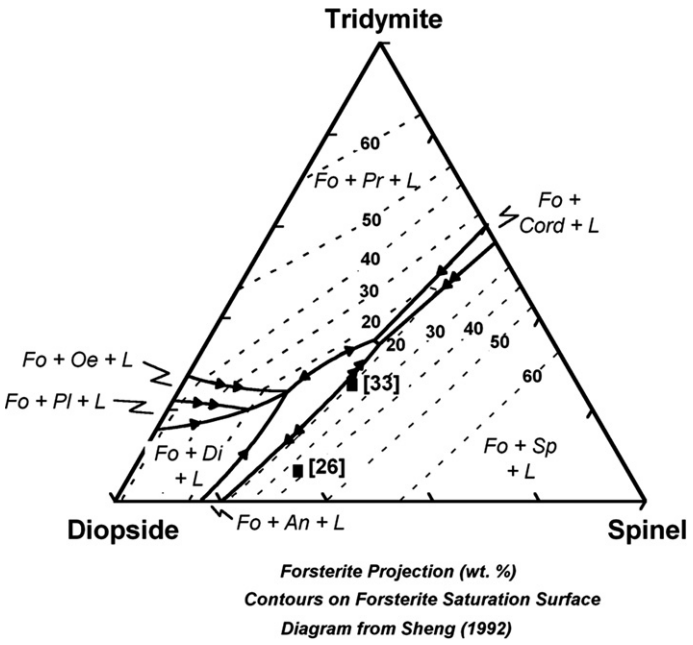

Fig. 3. The bulk compositions of OL1 and OL2, projected from forsterite onto the plane tridymite-diopside-spinel (from Sheng, 1992). Contours show the forsterite saturation surface, and the numbers in brackets show the forsterite coordinate for each composition ([33] is for OL2 and [26] is for OL1). Abbreviations as used previously except: Oe, orthoenstatite; Pi, pigeonite; Pr, protoenstatite; Sp, spinel.

are stubby in charges cooled slowly (5–50 °C/h) and more elongate at faster cooling rates. A clear exception to this pattern is run DynPL1#3 (see Fig. 5; $T_{max} = 1401$ °C, cooling rate = 10 °C/h), which was heated for 4 h instead of 3; this resulted in fewer surviving nuclei, a more coarse-grained texture relative to the runs cooled at 5 and 50 °C/h at the same T_{max}, and very elongate anorthite blades. This run is a clear demonstration of how T_{max} and heterogeneous nucleation (i.e., the number of nuclei) have more effect on texture than does cooling rate for this composition.

3.2.3. PL2 composition

The runs for composition PL2 show by far the most striking effect of T_{max} on textures (Fig. 6).

The runs started at $T_{max} = 1416$ °C (subliquidus, but above the anorthite first appearance temperature of 1379 °C) all have granular textures regardless of cooling rate. Crystals are numerous and small (rarely, up to 30 μm) even at slow cooling rates. Both forsterite and spinel crystals are ragged in shape, owing to their respective reaction relationships with the melt; the enstatite is the product of the forsterite reaction.

Run products from experiments started at $T_{max} = 1475$ °C ($\sim T_{liquidus}$) have very different textures from the runs started at $T_{max} = 1416$ °C and, also unlike the latter, show a very strong dependence on cooling rate. Anorthite dominates the textures and always occurs as elongate crystals, ranging from bladed phenocrysts in the slowest cooling rates (5–10 °C/h) to sheaves of radiating dendrites in the 500–1000 °C/h runs. Spinel occurs as small granules in most of the runs, regardless of cooling rate, but orthopyroxene and very small grains of olivine are confined to the variolitic mesostasis.

3.2.4. OL1 composition

In contrast with composition PL2, the run products for composition OL1 (Fig. 7) exhibit a stronger dependence on cooling rate than on T_{max}.

Experiments run started at $T_{max} = 1416$ °C (subliquidus; Fig. 7) have euhedral to subhedral forsterite crystals (up to 50–60 μm) and small granules of spinel (commonly having a thin reaction rim) enclosed in anorthite, pyroxene, and locally glass. With increasing cooling rates, the forsterite crystal shapes become more elongate. The overall textures range from granular (cooling rates 5–50 °C/h) to strongly porphyritic (olivine) at 100–1000 °C/h. At cooling rates of 100 °C/h and higher, the anorthite crystals become progressively finer-grained and distinctly elongate in shape; in these runs, the diopside clearly fills in interstices between the anorthite blades.

Runs that were started at $T_{max} = 1470$ °C (liquidus) exhibit a broadly similar range of textures to the runs started at $T_{max} = 1416$ °C textures, again ranging from granular at the slower cooling rates to strongly porphyritic (olivine) at the highest cooling rates. The principal differences between the two sets of experiments are the more variable olivine crystals shapes, finer grained mesostases, and a transition from granular to bladed anorthite at a lower cooling rate (50 vs. 100 °C/h) in the runs started at $T_{max} = 1470$ °C. Another, more subtle, difference is that in runs started at $T_{max} = 1416$ °C, the olivine crystals are uniformly scattered through the charge, whereas in runs started at $T_{max} = 1470$ °C there are numerous small equant grains developed around the edge of charges and fewer, larger, skeletal (especially at high cooling rates) crystals in the centers of the charges (Fig. 8). Numerous studies have reported preferential concentrations of grains near charge surfaces

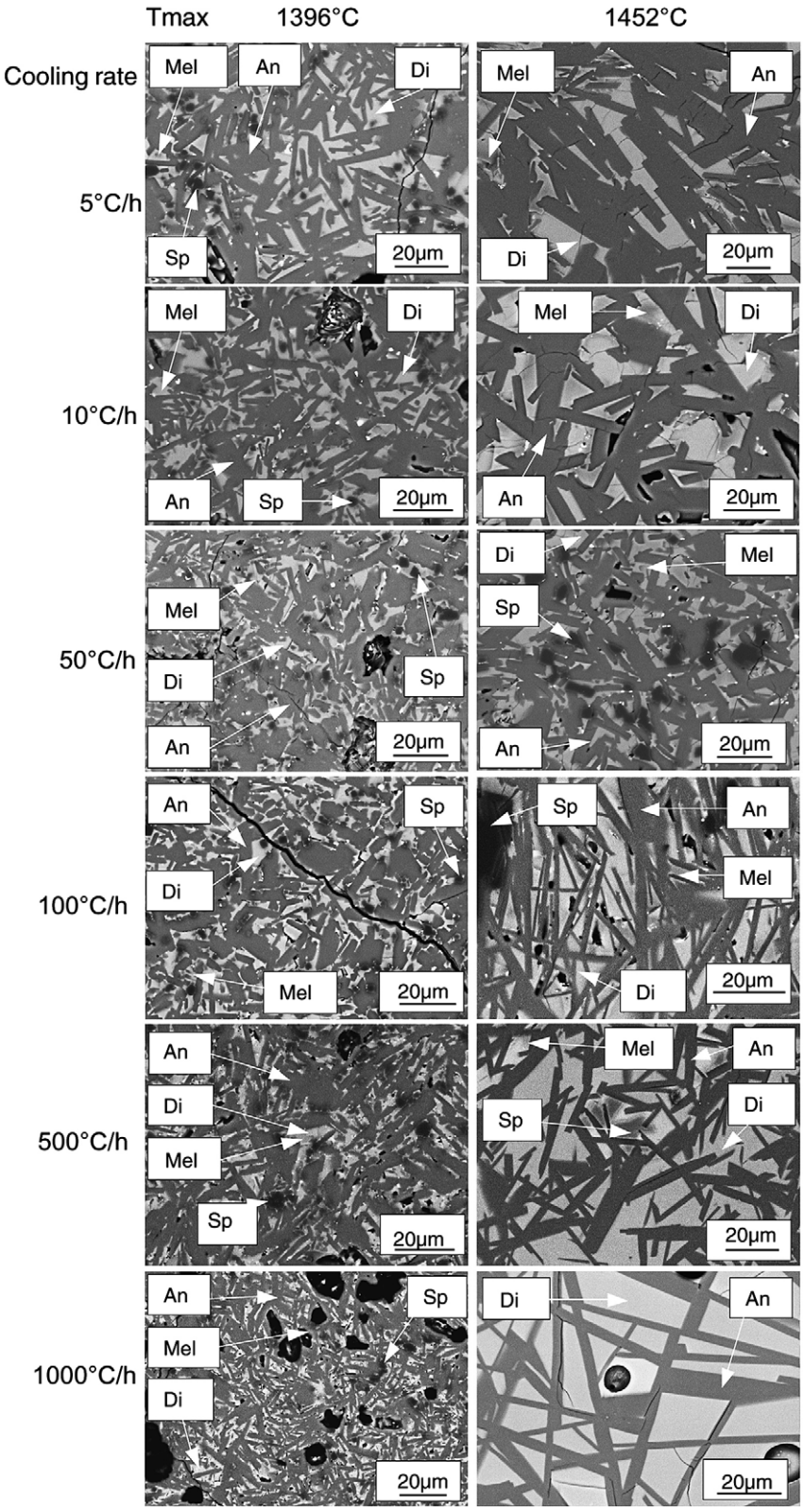

Fig. 4. B.s.e. images of dynamic crystallization experiments for type C CAI composition, comparing textures of runs cooled from two different starting temperatures (T_{max}) at cooling rates from 5–1000 °C/h. The textures in all cases are dominated by euhedral anorthite (An) blades with interstitial calcic clinopyroxene (cpyx). Runs started at higher T_{max} (right side) generally contain fewer, larger crystals than runs started at lower T_{max}. Circular and void structures in some runs, in this and other figures, are bubbles. Abbreviations as used previously.

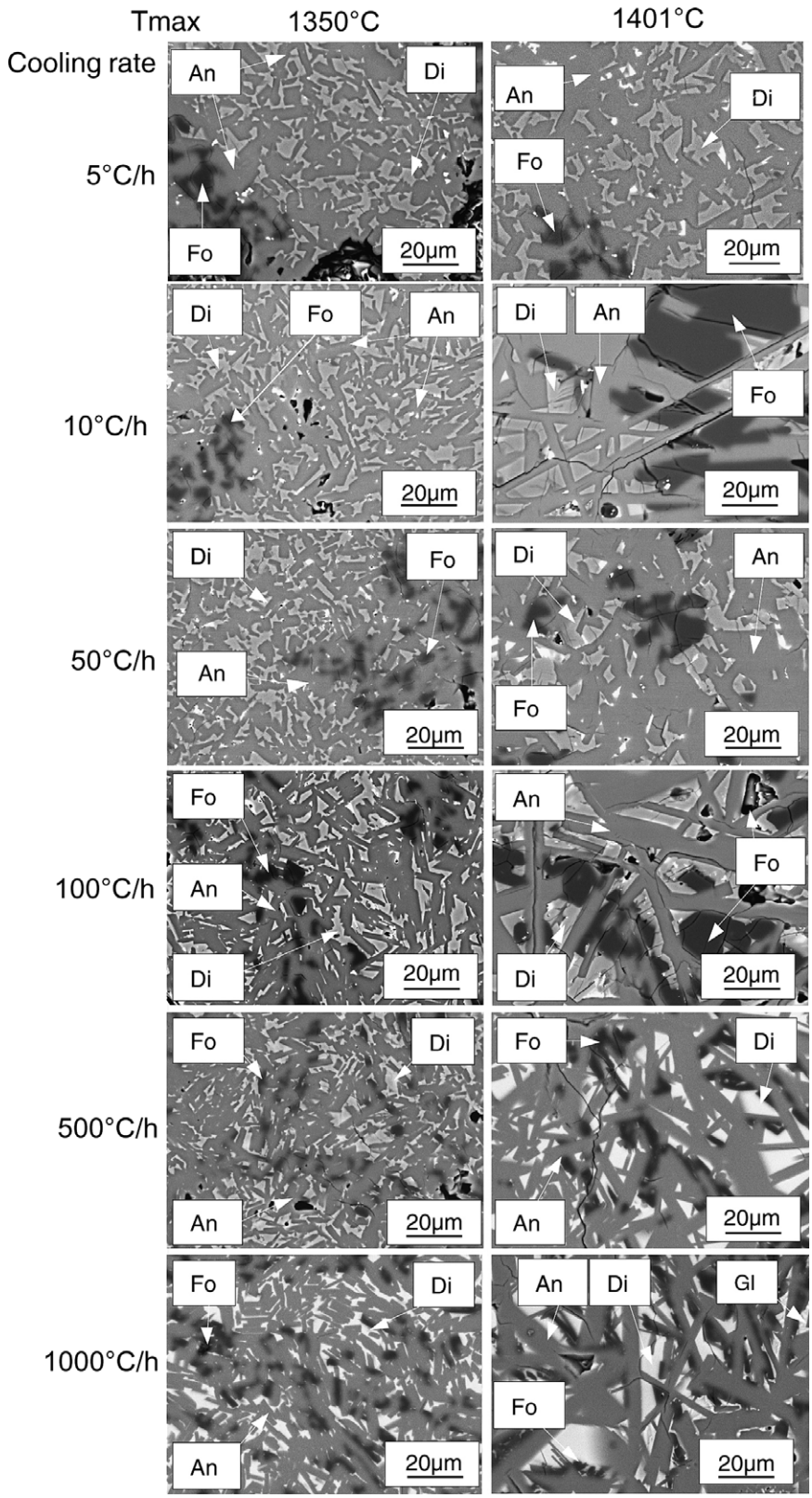

Fig. 5. B.s.e. images of dynamic crystallization experiments for PL1 composition, showing the results for two different T_{max} and a range of cooling rates as in Fig. 4. As for the Type C CAI composition, the textures are dominated by euhedral anorthite laths; unlike the Type C CAI composition, forsterite is an important phases in these runs. Although not shown in these photos, spinel also occurs in some runs for this bulk composition. Again, runs started at higher T_{max} have fewer, larger crystals than runs started at lower T_{max}. Abbreviations as used previously except: Gl, glass.

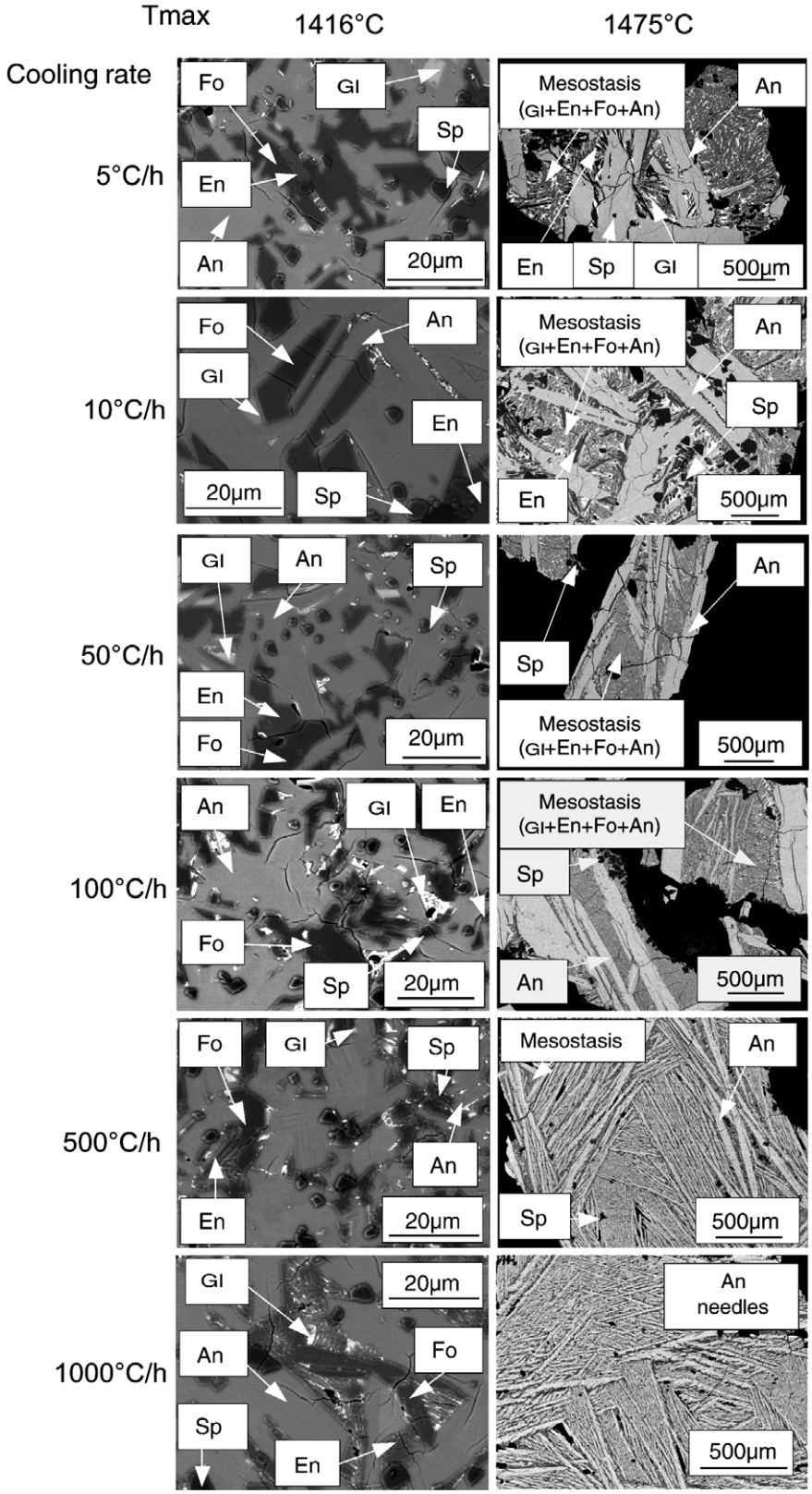

Fig. 6. B.s.e. images of dynamic crystallization experiments for PL2 composition, showing the results for two different T_{max} and a range of cooling rates as in Fig. 4. As discussed in the text, the runs cooled from $T_{max} = 1475$ °C have very different textures than those cooled from $T_{max} = 1416$ °C. Abbreviations as used previously except: En, enstatite.

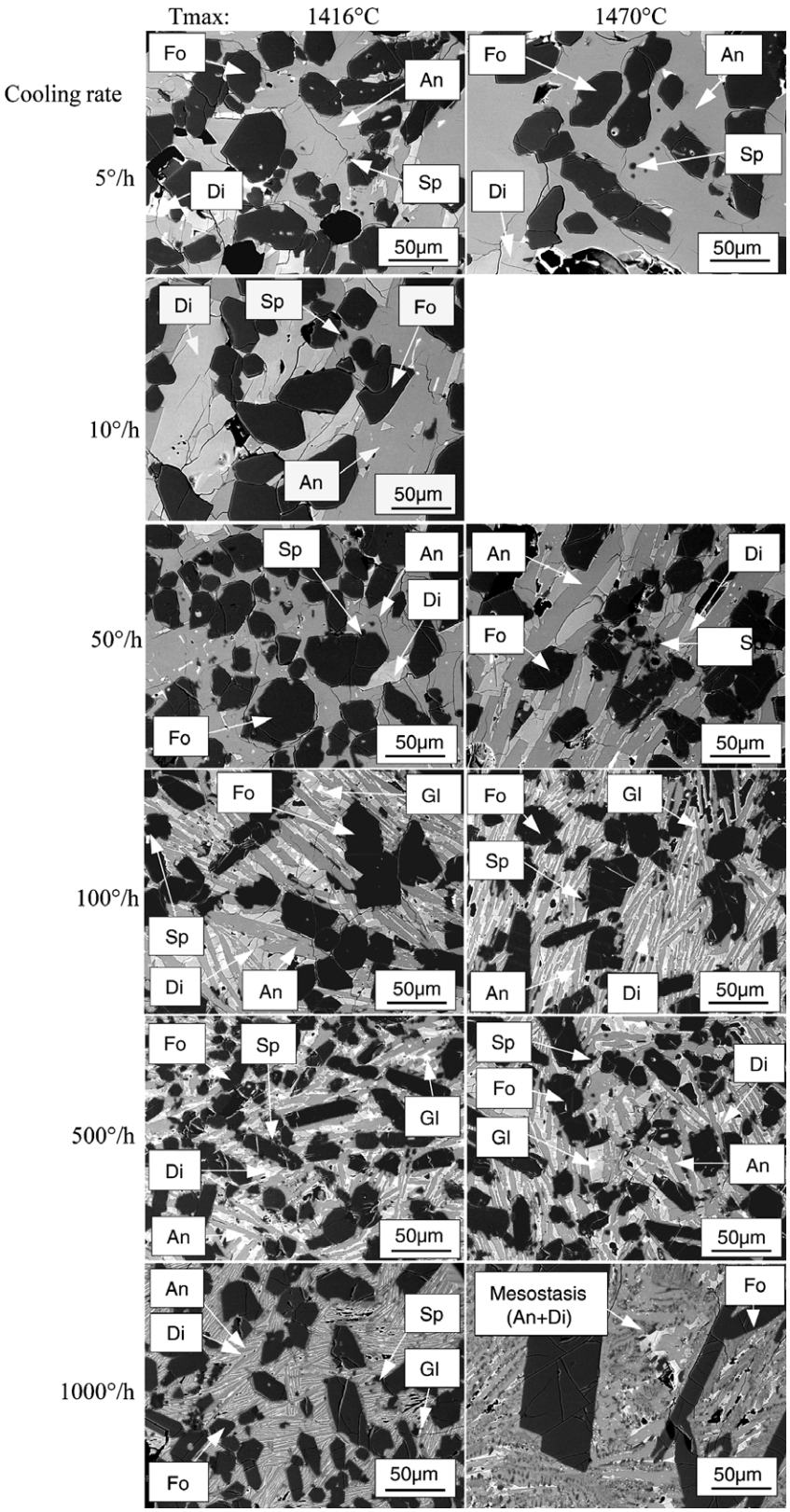

Fig. 7. B.s.e. images of dynamic crystallization experiments for OL1 composition, showing the results for two different T_{max} and a range of cooling rates as in Fig. 4. At the highest cooling rates the mesostases become extremely fine-grained and dominated by acicular and skeletal crystal forms.

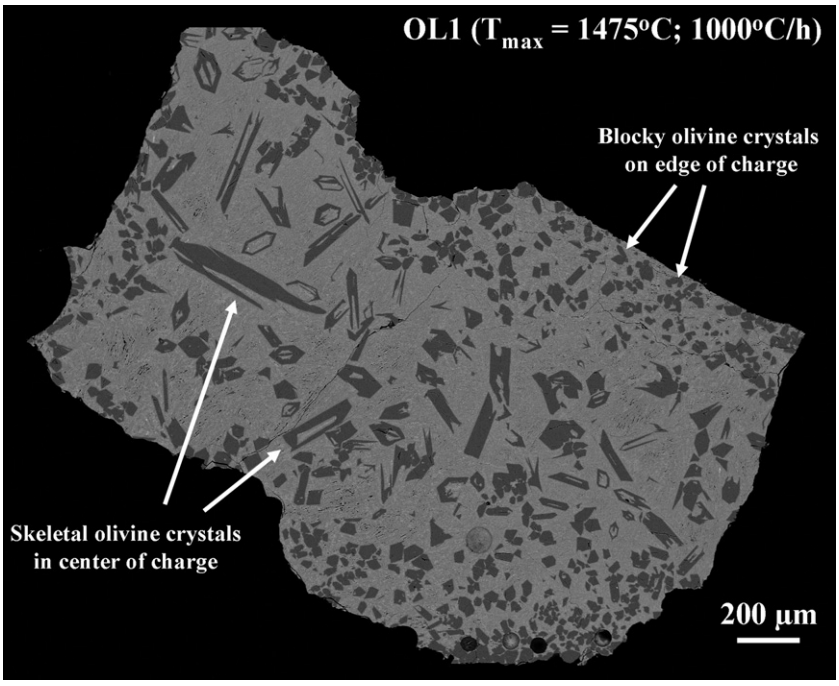

Fig. 8. B.s.e. image of the experimental charge OL1#11 (T_{max} = 1475 °C, cooling rate 1000 °C/h), showing a concentration of smaller equant grains around the periphery of the charge and fewer, larger and more skeletal crystals in the center.

(e.g., Lofgren and Russell, 1986), and the effect has been attributed to surface tension.

3.2.5. OL2 composition

Similar to composition OL1, the run products for composition OL2 (Fig. 9) exhibit a greater dependence on cooling rate than on T_{max}.

At a cooling rate of 10 °C/h, experiments starting with T_{max} = 1450 °C (subliquidus) have textures that are actually dominated by anorthite blades even though forsterite is the liquidus phase. With increasing cooing rate, the anorthite blades become much finer grained and forsterite phenocrysts dominate the texture, ranging in shape from euhedral and equant at 100 °C/h to highly skeletal at 1000 °C/h. At cooling rates above 100 °C/h, the very fine-grained mesostasis consists of feathery anorthite and interstitial glass.

Textures in runs started at T_{max} = 1502 °C (liquidus) exhibit a similar progression of textures as do the runs started at T_{max} = 1450 °C: they are granular at the lowest cooling rates (5 °C/h) and become increasingly porphyritic with increasing cooling rates. Again, the olivine crystals dominate the textures only at the higher cooling rates (>10 °C/h) and, again, become increasingly skeletal in shape with increasing cooling rate.

4. DISCUSSION

4.1. The separate effects of bulk composition, cooling rate, and T_{max}

Our experimental results clearly confirm the effects of bulk composition on mineralogy and textures in diverse Al-rich chondrule liquids, along the lines predicted by MacPherson and Huss (2005). The PL1 and PL2 compositions are both approximately plagioclase-saturated, yet the run products differ significantly even under the same conditions of cooling rate and T_{max} because the evolving liquids follow different paths owing to their respective positions relative to the thermal divide (Fig. 1). Similarly, OL1 and OL2 residual liquids evolve differently both from each other (thermal divide again) and from PL1 and PL2 in having early-formed forsterite instead of anorthite. The effects of cooling rate and T_{max} are superimposed on these first-order bulk-compositional differences. Similar conclusions were also reached for ferromagnesian chondrules by Tsuchiyama et al. (1980) and Lux et al. (1981).

T_{max} is a more important factor than cooling rate in controlling the textures of anorthite-rich compositions (Type C CAI, PL2, PL1) than it is for the two olivine rich compositions. We infer that this is due to the greater homogeneous nucleation difficulties for anorthite relative to forsterite. Type C CAI, PL2, and PL1 charges run at subliquidus starting temperatures contain greater numbers of, and smaller, crystals than in runs started from the liquidus, due clearly to reduced numbers of nuclei in the latter. For the olivine-rich compositions OL1 and OL2, however, the effects of cooling rate dominate because of the relative ease of nucleation of olivine and the great variation of olivine crystal shape with cooling rate.

The Type C CAI, PL1 and PL2 compositions are broadly similar in being very aluminous, and differ primarily in CaO (decreasing from Type C CAI to PL1 to PL2) and in MgO (Type C CAI is somewhat lower than PL1 or PL2). All three compositions have textures dominated

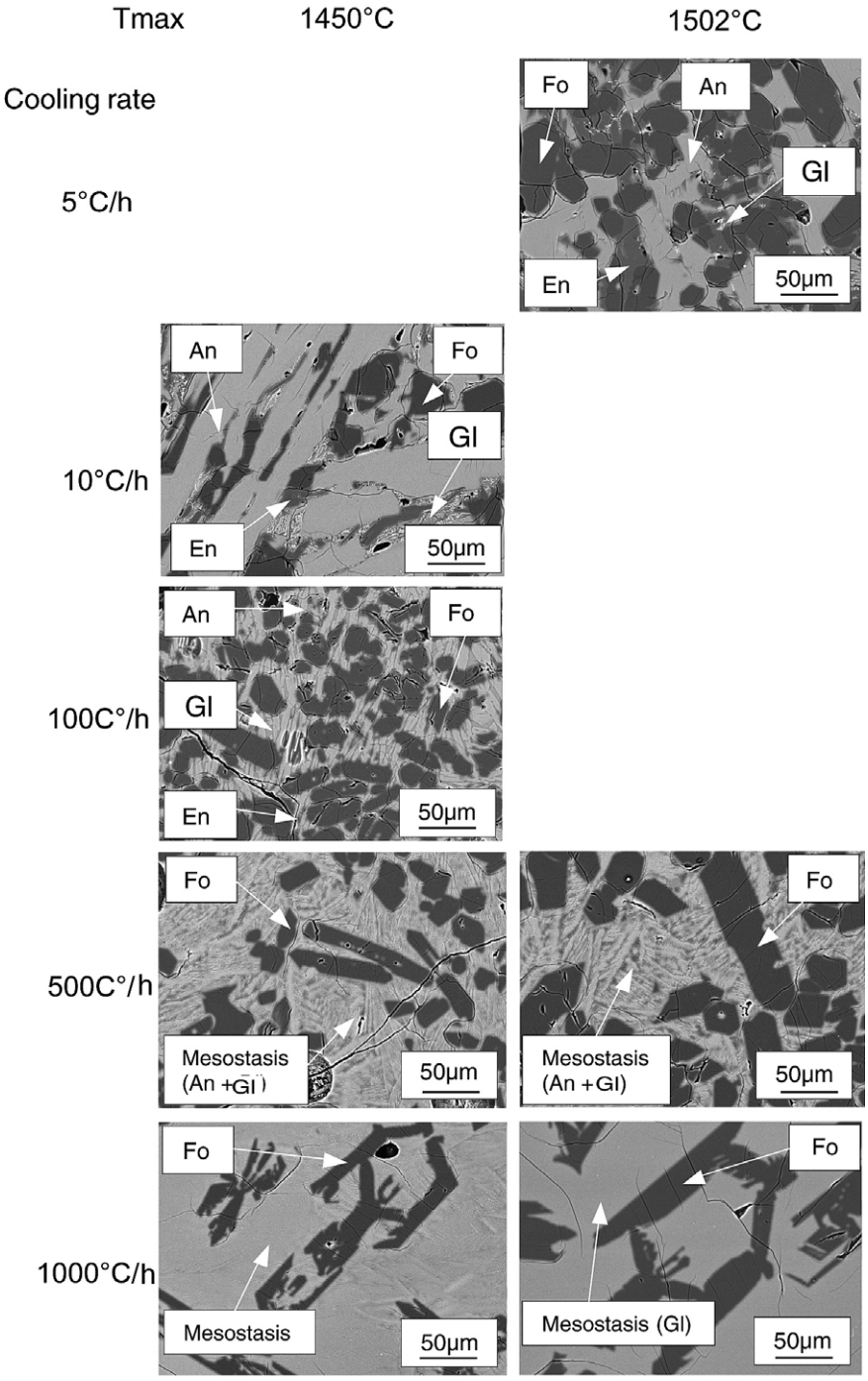

Fig. 9. B.s.e. images of dynamic c crystallization experiments for OL2 composition, showing the results for two different T_{max} and a range of cooling rates as in Fig. 4. With increasing cooling rate the olivine crystals go from equant to elongate to skeletal in shape. Abbreviations as used previously.

by early-formed anorthite. Observed textures in Type C CAI and PL1 experimental runs are similarly ophitic and exhibit similar dependencies on cooling rate and T_{max}. Anorthite laths become more elongate as cooling rate increases for both compositions, and for both compositions this variation is seen mainly for sets of experiments made with the higher (near-liquidus) starting temperatures. The principal differences between experiments on Type C CAI and PL1 composition are mineralogic: spinel + anorthite + melilite + diopside for Type C CAI, and anorthite + spinel (commonly reacted out) + forsterite + diopside for PL1. These differences are entirely to be expected, as the evolving Type C CAI melt will never intercept the forsterite crystallization field (Fig. 2; see also

MacPherson and Huss, 2005). Results of experiments on the PL2 composition are distinct from the Type C CAI and PL1 results, not just in modal mineralogy but also in showing a striking dependence on T_{max}. Experiments cooled from subliquidus temperature have textures fairly similar to PL1 textures despite somewhat different mineralogy (PL2 has modal enstatite and no diopside). For PL2 experiments started at the liquidus temperature however, the observed textures are completely different from those in PL1 because the anorthite entry temperature for the PL2 bulk composition is significantly lower than the liquidus temperature. The degree of supercooling required for anorthite nucleation is apparently rather large, such that when it does begin to crystallize it "sprouts" rapidly. Even at the slowest cooling rates the phenocrysts are markedly elongate and somewhat skeletal, and the textures change from porphyritic to radial plagioclase as cooling rate increases. We cannot rule out the possibility that textural variation with cooling rate could be similarly important in the Type C CAI and PL1 experiments if the latter were conducted at higher starting temperatures (liquidus and superliquidus T_{max}, respectively, for Type C CAI and PL1) than those we actually used.

OL1 and OL2 charges are very different from the three others, as expected from their strongly olivine-normative compositions. Both are consistently porphyritic. Relative to each other, the higher SiO_2 and lower CaO contents in the OL2 bulk composition result in modal enstatite that is absent in the OL1 charges. These two compositions exhibit a more consistent dependence on cooling rate variations than do the other three compositions. Especially this is apparent in the olivine crystal habits, but it also affects the textures in the pyroxene- and anorthite-rich mesostases, which range from crystalline at slow cooling rates to feathery or even glassy at the highest cooling rates.

Finally, our experiments also demonstrate the very important textural consequences of the number density of crystals or nuclei at the beginning of the crystallization, which is controlled primarily by T_{max}. This effect is most pronounced for anorthite-rich compositions, owing to the nucleation difficulties of that phase.

4.2. Comparison of our experimental results with natural aluminous chondrules

Our experimental results establish a matrix of mineralogical and textural properties for Al-rich chondrule melts that is a function of bulk composition, T_{max}, and cooling rate. Of course there are other parameters (e.g., heating time, precursor size, grain size, presence of other components such as Fe and Cr) that may have been significant for natural chondrules but which were not studied in our work, and we are especially mindful of a recent statement that "mineral zoning is a better guide to cooling rate than texture" (Hewins et al., 2005, p. 298). Nevertheless our experiments (even though they are Fe-free and hence do not have zoned crystals) permit for the first time constraining the formation conditions of natural Al-rich chondrules in a manner similar to what has been done for ferromagnesian chondrules and some types of CAIs. Of particular interest is whether Al-rich chondrules can be associated with formation conditions akin to CAIs or, alternatively, to those of ferromagnesian chondrules.

With that end in mind, in this section we make detailed comparison between our charges and specific well-characterized Al-rich chondrules. Recalling that MacPherson and Huss (2005) defined four fundamental types of Al-rich chondrules separated by a boundary curve and a thermal divide, and upon which our experimental compositions are based, we have selected "case studies" of each variety of natural chondrule with which to compare our results. Some of these illustrate the agreement between observations and experiments, while others have apparent discrepancies that in fact demonstrate the need for other factors to be considered including, in some cases, likely small errors in calculating the bulk compositions of the natural chondrules. There exist several isotopic and petrographic studies of Al-rich chondrules (Bischoff and Keil, 1983a,b; Bischoff and Keil, 1984; Bischoff et al., 1985, 1989; Russell et al., 2000; Krot and Keil, 2002a,b; MacPherson and Huss, 2005) that enable such comparisons. Fig. 10 shows the compositions of our "case-study" Al-rich chondrules plotted on the same diagram as that in Figs. 1 and 2. In the discussion that follows, we necessarily assume closed-system behavior and (again) we emphasize the possible roles of other parameters as noted above. Volatile loss (or gain) in particular is a relatively unknown parameter that could have large effects, as it would affect crystallization temperatures and textures (e.g., Alexander, 1996; Cohen et al., 2004).

4.2.1. Chainpur 1251-14-1

This chondrule was first described by Russell et al. (1996) and later studied in detail by MacPherson and Huss (2005). Using the nomenclature of the latter authors, this is an example of an Al-rich [Oliv] chondrule. Fig. 11a illustrates its porphyritic texture, with euhedral equant olivine crystals and a large spinel grain in a matrix of elongate plagioclase laths, interstitial diopside, and minor Fe–Ni metal. The bulk composition and mineralogy of this chondrule are very similar to those of our composition OL1. The texture is remarkably similar to that in experimental charges that resulted from cooling composition OL1 at 100–500 °C/h from both $T_{max} = 1416$ °C and $T_{max} = 1470$ °C. Fig. 11b illustrates run DynOL1#10 (Table 3), which was cooled at 500 °C/h from $T_{max} = 1416$ °C (subliquidus). Charges cooled more slowly from either T_{max} have coarser textures and blockier anorthite crystals than the natural chondrule. Charges cooled more rapidly from either T_{max} have very fine grained mesostases with dendritic textures that are unlike those in Chainpur 1251-14-1. Of course other properties such as mineral zoning in an iron-bearing system would further constrain the cooling rates but, based on our results in the iron free system, the observed properties of Chainpur chondrule 1251-14-1 are consistent with closed-system heating of the precursor to a temperature 10–64 °C below the liquidus (estimated at 1480 ± 18 °C) and subsequent cooling at 100–500 °C/h.

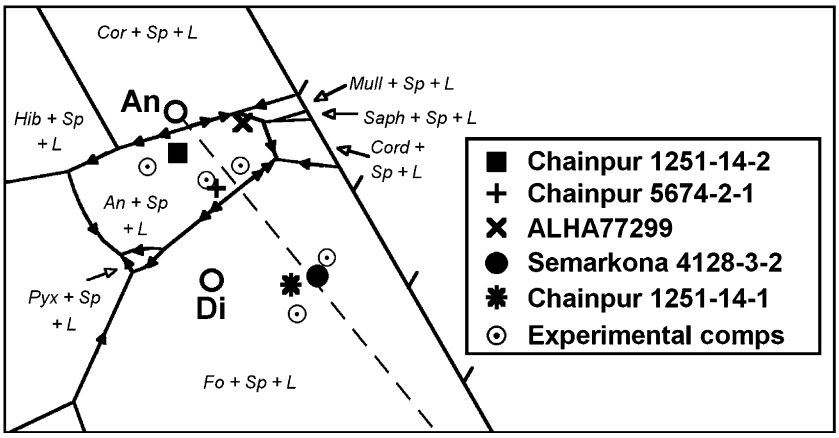

Fig. 10. Compositions of several "case study" natural Al-rich chondrules (Bischoff and Keil, 1983a,b; Russell et al., 1996; MacPherson and Huss, 2005), plotted as in Fig. 2, together with the experimental compositions used in this study. Abbreviations as used previously.

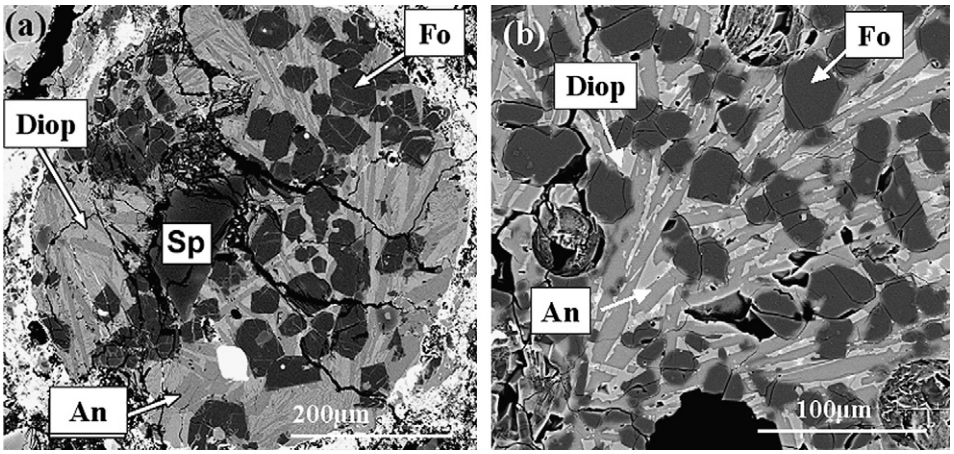

Fig. 11. Comparison between the natural chondrule 1251-14-1 (a) from Chainpur (photo from MacPherson and Huss, 2005) and the experimental charge OL1#10 (b) with a maximum temperature of 1416 °C and a 500 °C/h cooling rate. Circular structures in (b) are bubbles.

4.2.2. ALHA77299 #20

Bischoff and Keil (1983a) first described this example of an Al-rich [Plag] chondrule (Fig. 12a). It has a porphyritic texture dominated by long laths of plagioclase and a single large spinel grain, set in a very fine-grained mesostasis. The bulk composition of this chondrule plots in the anorthite (+spinel) primary phase volume on Fig. 10, broadly similar to our experimental composition PL2. Its textural properties are similar to our experimental runs in which composition PL2 was cooled from near the liquidus at $T_{max} = 1475$ °C at cooling rates of 50–100 °C/h (Fig. 12b shows the 100 °C/h run). Runs starting at $T_{max} = 1475$ °C but cooled more slowly (5–10 °C/h) have coarser plagioclase laths; runs cooled at 500 and 1000 °C/h cooling rates have radial plagioclase textures (e.g., see Fig. 6). Experimental runs that started at $T_{max} = 1416$ °C (subliquidus) differ in having granular textures at all cooling rates, unlike those in the natural chondrule.

The properties of ALHA77299 #20 are consistent with precursor melting at near-liquidus temperatures (estimated around 1478 °C) followed by cooling at 50–100 °C/h.

4.2.3. Chainpur 5674-2-1

This Al-rich [Plag] chondrule was studied previously by Russell et al. (1996) and MacPherson and Huss (2005). Its texture is dominated by large plagioclase laths (Fig. 13a), some of which are partly to completely replaced by nepheline. Blocky to skeletal olivine crystals are mostly external to the plagioclase laths. Interstitial to the plagioclase laths and olivine crystals is an unusual dendritic to variolitic intergrowth of aluminous diopside, olivine, and fine-grained plagioclase laths. Like chondrule ALHA77299 #20 above, the bulk composition of Chainpur 5674-2-1 plots in the anorthite (+spinel) primary phase volume on Fig. 10 but on the opposite side of the anorthite–forsterite tie line; it is similar in composition to our experimental composition PL1.

None of our experimental runs produced anything like the unusual feathery mesostasis texture seen in the natural chondrule. The closest approach to the natural chondrule textures was obtained in runs begun at $T_{max} = 1401$ °C (near-liquidus), and of these only the runs with the most rapid cooling rates (500–1000 °C/h) produced elongate and

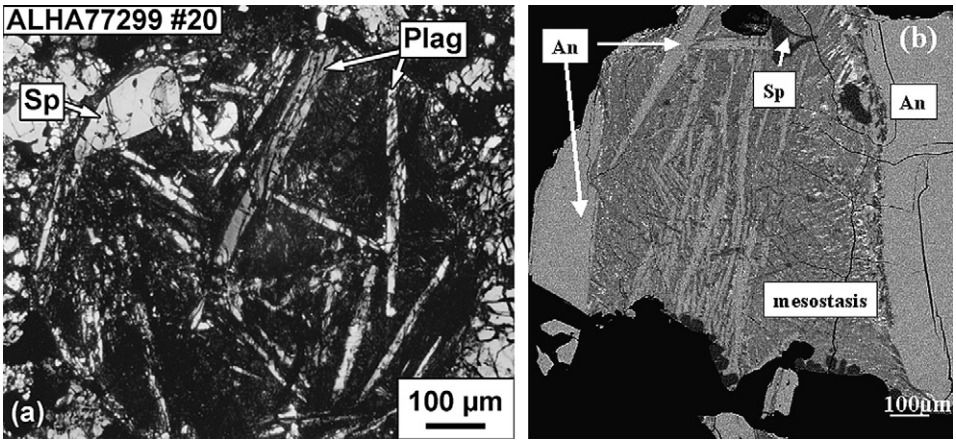

Fig. 12. Comparison between (a) the natural Al-rich chondrule ALHA77299 #20 (photo courtesy of A. Bishoff; see Bischoff and Keil, 1983a) and (b) the experimental charge PL2#7, cooled from a maximum temperature of 1475 °C at 100 °C/h.

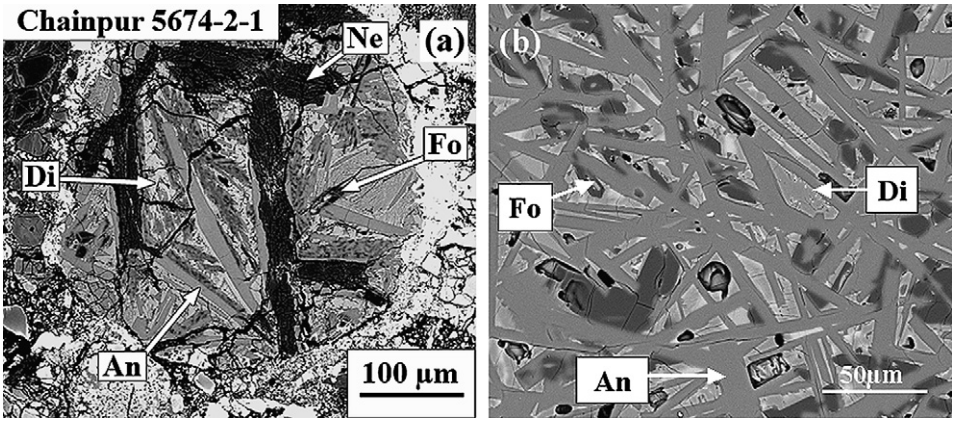

Fig. 13. Comparison between (a) the natural Al-rich chondrule Chainpur 5674-2-1 (photo from MacPherson and Huss, 2005) and (b) the experimental charge PL1#7, cooled from a maximum temperature of 1401 °C at 100 °C/h.

slightly skeletal forsterite crystals (Fig. 13b). All of the PL1 runs started at subliquidus temperatures ($T_{max} = 1350$ °C) contain stubby plagioclase crystals and a fine-grained granular texture, regardless of cooling rate.

Although not a perfect match, our experiments suggest that this chondrule most likely formed as a result of precursor melting at near-liquidus temperatures (1401 ± 8 °C) followed by relatively rapid cooling at ⩾500 °C/h.

4.2.4. Chainpur chondrule 1251-14-2

This Al-rich [Plag] chondrule was described by Russell et al. (1996) and MacPherson and Huss (2005); it is illustrated here in Fig. 14a. It is broadly similar to Chainpur 5674-2-1 in bulk composition and texture, and thus also is similar in composition to our PL1. Like 5674-2-1, it contains large plagioclase laths that are partially replaced by nepheline, with a mesostasis composed of a tangle of plagioclase and aluminous diopside. What makes this chondrule different from Chainpur 5674-2-1 is the fact that its mineralogy does not match the expectations of phase equilibria: olivine—an expected phase for this bulk composition—is lacking. All of our PL1 charges show textures dominated by plagioclase laths and all contain olivine (e.g., Fig. 14b), which is not the case for Chainpur 1251-14-2. MacPherson and Huss (2005) attributed this unexpected absence of olivine either to a small error in the determination of the composition (underestimate of pyroxene, which would make it effectively a Type C CAI) or else to a very rapid cooling rate that resulted in metastable enlargement of the pyroxene field. Our results are inconsistent with this last hypothesis, because even at a cooling rate of 1000 °C/h our charges contain a lot of olivine. The critical clue comes from examination of Fig. 10, which shows that the composition of Chainpur 1251-14-2 plots very close to the line connecting the mineral anorthite with the distributary reaction point where the forsterite–anorthite reaction curve hits the pyroxene field. Only a slight underestimation of the pyroxene content, as suggested by MacPherson and Huss (2005) would shift its composition to the other side of the line into the Type C CAI field; a melt of such composition would never crystallize forsterite. Thus the apparent inconsistency between the observed mineralogy of Chainpur 1251-14-2 and that expected from phase equilibria actually illustrates the effect that even a small error in bulk composition can have.

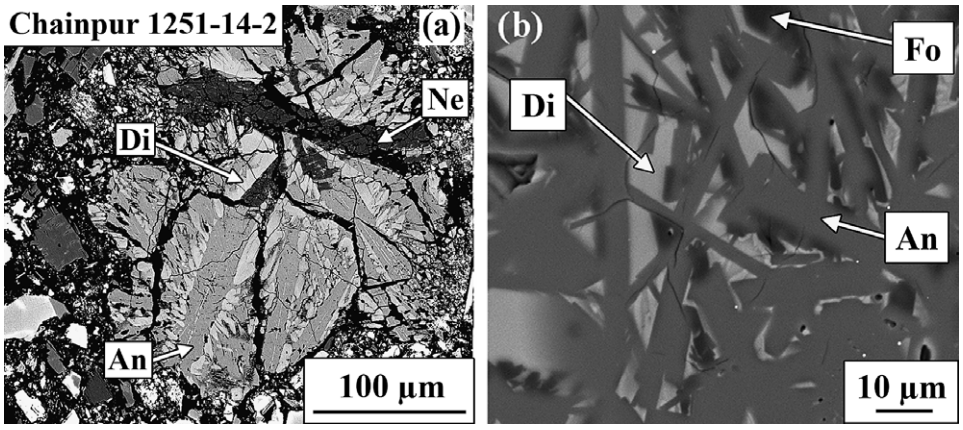

Fig. 14. Comparison between (a) the natural Al-rich chondrule Chainpur 1251-14-2 (see MacPherson and Huss, 2005) and (b) the experimental charge PL1#11, cooled from a maximum temperature of 1401 °C at 1000 °C/h.

Setting aside the "missing olivine", the closest approach in our experiments to the textures in the natural chondrule are those cooled from the liquidus temperature (1401 °C) at the most rapid cooling rates (e.g., Fig. 14b). Note that even these, however, do not show the feathery diopside crystal forms observed in the natural chondrule.

4.2.5. Semarkona 4128-3-2

This Al-rich [Oliv] chondrule (Fig. 15a) was first studied by Russell et al. (1997); it has a bulk composition that lies on the opposite side of, but very close to, the anorthite–forsterite tie line from Chainpur 1251-14-1 and is analogous to our experimental composition OL2. Its partly barred texture is dominated by olivine crystals, with interstitial plagioclase, aluminous diopside, and minor spinel and glass (MacPherson and Huss, 2005).

For the most part the observed crystallization sequence is consistent with the runs for composition OL2. The main difference is that the bulk composition of this chondrule is such that low-calcium pyroxene should be a very late-crystallizing igneous phase (after olivine, spinel, and anorthite), yet this phase is absent (MacPherson and Huss, 2005). Most of the dynamic crystallization run products from OL2 do contain low calcium pyroxene as expected, with the exception of those cooled at the highest cooling rates (Table 3). This may be another example where a very small error in bulk composition determination (e.g., if the thin section slice is not precisely representative of the whole chondrule) might erroneously shift the bulk composition to the other side of the forsterite–anorthite tie line. Alternatively, the natural chondrule may have cooled sufficiently rapidly that the low-Ca pyroxene never appeared. Yet a third alterative was proposed by MacPherson and Huss (2005), who noted that the small amount of sodium in this chondrule (the plagioclase is An_{83}) has the effect of shifting the thermal divide slightly compared to the same composition without sodium. This shift will in principle cause the residual liquid to evolve toward diopside instead of low calcium pyroxene, although we have not investigated the effect experimentally.

None of our experimental runs using OL2 produced anything like a barred texture in the olivines that could be compared to Semarkona 4128-3-2, which may be expected given that none of our dynamic crystallization runs

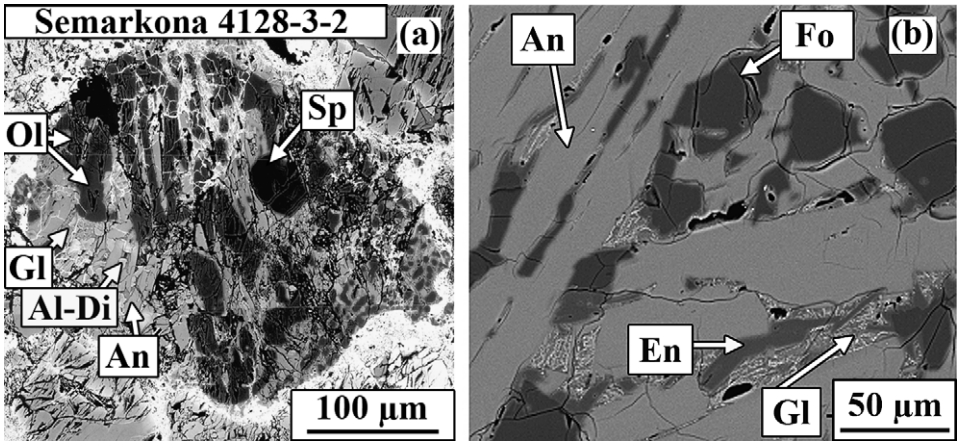

Fig. 15. Comparison between (a) the natural chondrule Semarkona 4128-3-2 (see MacPherson and Huss, 2005) and (b) the experimental charge Ol2#4 cooled from a maximum temperature of 1450 °C at 10 °C/h.

was begun at the strongly super-liquidus temperatures that are thought necessary to produce barred olivine textures (e.g., Hewins et al., 2005). Under the conditions of our experiments, markedly skeletal olivine forms were produced at a cooling rate of 1000 °C/h, independent of T_{max}. Curiously, however, the groundmass textures of Semarkona 4128-3-2 are most closely approximated in our experiments run at the *lowest* cooling rates (e.g., Fig. 15b): at cooling rates of 100 °C/h and above, the mesostases of all run products independent of T_{max} are either dendritic or glassy. Blocky plagioclase crystal shapes like those in the natural chondrule are observed in our experiments only at cooling rates $\leqslant$10 °C/h. Regardless of the conditions necessary to form barred olivines, the groundmass textures of Semarkona 4128-3-2 may be consistent with low cooling rates at the lowest temperatures, i.e., non-linear cooling as suggested by Weinbruch et al., 2001.

4.2.6. Formation conditions of Al-rich chondrules

To first order, the results of our experiments support the proposal of MacPherson and Huss (2005) that the combination of the thermal divide (centered on the forsterite–anorthite tie line) and the spinel-saturated anorthite–forsterite boundary curve naturally divide Al-rich chondrules into four basic types. In addition, comparison of natural chondrule textures with those of the relevant experimental charges run under a range of well-defined conditions have allowed us to place constraints the formation conditions of the natural chondrules. Based on such comparisons as detailed above, and assuming that the chondrules have liquidus temperatures similar to our respective chosen bulk compositions, many of the natural objects experienced melting at near- and sub-liquidus temperatures (~1400–1475 °C) followed by (probably non-linear) cooling at 50–500 °C/h.

Barred olivine textures (BO) require somewhat different conditions that are outside of the range of our experiments. Although BO chondrules account for only 5–10% of chondrules in general (Grossman et al., 1988), they are more numerous for aluminous chondrules (up to 20%). Russell et al. (1996; illustrated in their Fig. 1D) described one such object, Inman 5652-1-1, that is very similar in bulk composition to Chainpur 1251-14-1 but has a very different texture consisting of barred olivine crystals that are cross cut by a coarsely bladed interstitial intergrowth of anorthite and aluminous diopside. We produced somewhat similar mesostasis textures for composition OL1 cooled from both liquidus and subliquidus temperatures at rates of 100–1000 °C/h. Recently, Tsuchiyama et al. (2004) succeeded in reproducing all kinds of BO textures with olivine rims, for normal ferromagnesian compositions, by heating at 100–200 °C above the liquidus temperature for 10 min followed by cooling at 500–1000 °C/h. Although we did not heat any of our experiments to strongly super-liquidus temperatures, nonetheless our inferred cooling rates for Inman 5652-1-1 (the mesostasis at least) are broadly consistent with the results of Tsuchiyama et al. (2004) for ferromagnesian compositions.

The peak melting temperatures of Al-rich chondrules (T_{max} ~ 1400–1500 °C), are distinctly higher than those of CAIs that have been studied by similar experimental techniques; the maximum temperature experienced by Type B CAIs was probably lower than 1400 °C (Stolper, 1982; Stolper and Paque, 1986). Also, the inferred cooling rates of Al-rich chondrules (up to 500 °C/h) are faster than determined for the Type B CAIs, which are in the range 0.5–50 °C/h (Stolper, 1982; Stolper and Paque, 1986). Al-rich chondrules formed at peak temperatures that overlap, but are at the low end of, those inferred for porphyritic ferromagnesian chondrules: a recent review by Hewins et al. (2005) placed the range for the latter as T_{max} ~ 1400–1850 °C (1500–1850 °C for rapid heating, and 1400–1600 °C with extensive evaporation), with cooling rates at 10–1000 °C/h. Therefore the conditions under which Al-rich chondrules formed are more closely related to those of normal ferromagnesian chondrules than to those of CAIs.

Our results are obviously just a first step in understanding the petrogenesis of a group of objects that represent a critical link between ferromagnesian chondrules and CAIs. A wider range of formational parameters (e.g., melt evaporation) needs to be explored, and more complex thermal histories than those employed here likewise must be investigated.

Our results do not place any significant constraints on the formation of Type C CAIs. All of the runs for this composition have ophitic textures consistent with those of natural Type C CAIs, regardless of cooling rate, although the grain size and grain density of the runs cooled from T_{max} = 1452 °C are closest to the natural inclusions. Unlike the Type B1 CAIs in which the dominant early crystallizing phase (melilite) is a solid solution whose zoning patterns help to constrain cooling rates (e.g., MacPherson et al., 1984), the anorthite in the Type C CAIs is not similarly zoned. Therefore, although we can conclude that the possible cooling rate space for Type C CAIs includes at least 5–1000 °C/h, we cannot place any limits. Our experiments for this composition suggest that if Type C CAIs cooled from subliquidus temperatures as did Type B CAIs (Stolper and Paque, 1986), the temperature was not too far below the liquidus (e.g., 1452 °C). However, an essential future experiment will be to conduct dynamic crystallization experiments on Type C CAI composition where T_{max} is well above the liquidus temperature.

5. CONCLUSIONS

Dynamic crystallization experiments performed on Al-rich chondrule analogue compositions show variable textures (ophitic, granular, porphyritic, radial plagioclase) that depend primarily on composition and to a lesser extent on degree of melting and cooling rate. Our results emphasize the important role of bulk composition, because with the same thermal history different bulk compositions achieve very different textures. Assuming closed system formation, peak temperatures of ~1400–1500 °C, and cooling rates of 50–500 °C/h are appropriate for most porphyritic Al-rich chondrules, conditions similar to those for ferromagnesian chondrules. Barred olivine examples probably required super-liquidus heating outside of the range of our experiments, and may have experienced somewhat faster cooling rates, up to ~1000 °C/h, relative to their porphyritic kin.

ACKNOWLEDGMENTS

We thank Bosmat Cohen, Omar Boudouma, Frédéric Couffignal, Michel Fialin, Harold Connolly, and Jerry Delaney, for discussions and especially for assistance with the experimental and analytical aspects of the study. Emma Bullock provided invaluable assistance in using the Smithsonian field emission SEM to study the run products. Addi Bischoff provided useful documentation and background on his earlier work on Al-rich chondrules. Finally, very constructive and helpful reviews by Gary Huss, Harold Connolly, and Addi Bischoff, plus the patience and helpful suggestions of A.E. Sara Russell, all greatly improved the manuscript. This research was supported in part by NASA Cosmochemistry grants NNG05GK11G (R. Hewins, P.I.) and NNG04GK47G (G. MacPherson, P.I.).

REFERENCES

Alexander C. M. O'D. (1996) Recycling and volatile loss in chondrule formation. In *Chondrules and Protoplanetary Disk* (eds. R. H. Hewins, R. H. Jones, and E. R. D. Scott). Cambridge University press, pp. 233–241.

Bischoff A. and Keil K. (1983a) Catalog of Al-rich chondrules, inclusions and fragments in ordinary chondrites. Special Publication No. 22, University of New Mexico, Institute of Meteoritics, Albuquerque, pp. 1–33.

Bischoff A., and Keil K. (1983b) Ca-Al-rich chondrules and inclusions in ordinary chondrites. *Nature* **303**, 588–592.

Bischoff A., and Keil K. (1984) Al-rich objects in ordinary chondrites: related origin of carbonaceous and ordinary chondrite and their constituents. *Geochim. Cosmochim. Acta* **48**, 693–709.

Bischoff A., Keil K., and Stoffler D. (1985) Perovskite-hibonite-spinel-bearing inclusions and Al-rich chondrules and fragments in enstatite chondrites. *Chem. Erde* **44**, 97–106.

Bischoff A., Palme H., and Spettel B. (1989) Al-rich chondrules from the Ybbsite H4 chondrite: evidence for formation by collision and splashing. *Earth Planet. Sci. Lett.* **93**, 170–180.

Blander M., Planner H. N., Keil K., Nelson L. S., and Richardson N. L. (1976) The origin of chondrules: experimental investigation of metastable liquids in the system Mg_2SiO_4–SiO_2. *Geochim. Cosmochim. Acta* **40**, 889–892.

Cohen B. A., Hewins R. H., and Alexander C. M. O'D. (2004) The formation of chondrules by open-system melting of nebular condensates. *Geochim. Cosmochim. Acta* **68**, 1661–1675.

Connolly, Jr., H. C., and Hewins R. H. (1991) The influence of bulk composition and dynamic melting conditions on olivine chondrule texture. *Geochim. Cosmochim. Acta* **55**, 2943–2945.

Grossman J. N., Rubin A. E., Nagahara N., and King E. A. (1988) Properties of chondrules. In *Meteorites and the Early Solar System* (eds. J. F. Kerridge and M. S. Matthews). University of Arizona, pp. 680–696.

Hewins R. H., and Radomsky P. M. (1990) Formation condition of pyroxene-olivine and magnesian olivine chondrules. *Geochim. Cosmochim. Acta* **54**, 3475–3490.

Hewins R. H. and Connolly H. C. Jr. (1996) Peak temperatures of flash-melted chondrules. In *Chondrules and the Protoplanetary Disk* (eds. R. H. Hewins, R. H. Jones, and E. R. D. Scott). Cambridge University Press, pp. 197–204. 346 pp.

Hewins R. H., Connolly H. C. Jr., Lofgren G. E., and Libourel G. (2005) Experimental constraints on chondrule origins. In *Proceedings of the Astrophysical Society of the Pacific Conference Series*, vol. 341, pp. 286–316.

Hsu W., Huss G. R., and Wasserburg G. J. (2003) Al-Mg Systematics of CAIs, POIs and ferromagnesian chondrules from Ningqiang. *Meteorit. Planet. Sci.* **38**, 35–48.

Jones R. H. (1990) Petrology and mineralogy of type II, FeO-rich chondrules in Semarkona (LL3.0): origin by closed-system fracional crystallization, with evidence for supercooling. *Geochim. Cosmochim. Acta* **54**, 1785–1802.

Jones R. H. (1994) Petrology of FeO-poor, porphyritic pyroxene chondrules in the Semarkona chondrite. *Geochim. Cosmochim. Acta* **l58**, 5325–5340.

Jones R. H., and Scott E. R. D. (1989) Petrology and thermal history of Type IA chondrules in the Semarkona (LL3.0) chondrite. *Proc. 19th Lunar Planet. Sci. Conf.*, 523–536.

Krot A. N., and Keil K. (2002a) Anorthite-rich chondrules in CR and CH carbonaceous chondrites: genetic link between calcium-aluminium-rich inclusions and ferromagnesian chondrules. *Meteorit. Planet. Sci.* **37**, 91–111.

Krot A. N., and Keil K. (2002b) Plagioclase-rich chondrules in the reduced CV chondrites: evidence for complex formation history and genetic links between calcium-aluminium-rich inclusions and ferromagnesian chondrules. *Meteorit. Planet. Sci.* **37**, 155–182.

Krot A. N., McKeegan K. D., Russell S. S., Meibom A., Weisberg M. K., Zipfel J., Krot T. V., Fagan T. J., and Keil K. (2001a) Refractory calcium-aluminum-rich inclusions and aluminum-diopside-rich chondrules in the metal-rich chondrites Hammadah al Hamra 237 and Queen Alexandra Range 94411. *Meteorit. Planet. Sci.* **36**, 1189–1216.

Krot A. N., Petaev M. I., Keil K., and Russell S. S. (2001b) Anorthite-rich chondrules in carbonaceous chondrites: significance for understanding the astrophysical setting of CAI and chondrule formation. *Meteorit. Planet. Sci. Supplement* **36**, A107.

Krot A. N., Hutcheon I. A., and Keil K. (2002) Plagioclase-rich chondrules in the reduced CV chondrites: evidence for complex formation history and genetic links between calcium-aluminum-rich inclusions and ferromagnesian chondrules. *Meteorit. Planet. Sci.* **37**, 155–182.

Krot A. N., Fagan T. J., Keil K., McKeegan K. D., Sahupal S., Hutcheon I. D., Petaev M. I., and Yurimoto H. (2004a) Ca, Al-rich inclusions, amoeboid olivine aggregates, and Al-rich chondrules from the unique carbonaceous chondrite Acfer 094: I. Mineralogy and petrology. *Geochim. Cosmochim. Acta* **68**, 2167–2184.

Krot A. N., Petaev I., and Yurimoto H. (2004b) Amoeboid olivine aggregates with low-Ca pyroxenes: a genetic link between refractory inclusions and chondrules? *Geochim. Cosmochim. Acta* **68**, 1923–1941.

Lofgren G. E. (1989) Dynamic crystallization of chondrule melts of porphyritic olivine composition: textures experimental and natural. *Geochim. Cosmochim. Acta* **53**, 461–470.

Lofgren G. E. (1996) A dynamic crystallization model for chondrule melts, In *Chondrules and Protoplanetary Disk* (eds. R. H. Hewins, R. H., Jones, and E. R. D. Scott). Cambridge University press, pp 187–196.

Lofgren G. E., and Russell S. S. (1986) Dynamic crystallization of chondrule melts of porphyritic and radial pyroxene composition. *Geochim. Cosmochim. Acta* **53**, 461–470.

Lofgren G. E., and Lanier A. B. (1990) Dynamic crystallization study of barred olivine chondrules. *Geochim. Cosmochim. Acta* **54**, 3537–3551.

Lux G., Taylor G. J., and Keil K. (1981) Chondrules in H3 chondrites: textures, compositions and origins. *Geochim. Cosmochim. Acta* **45**, 675–685.

MacPherson G. J., Paque J. M., Stolper E., and Grossman L. (1984) The origin and significance of reverse zoning in melilite from Allende Type B inclusions. *J. Geol.* **92**, 289–305.

MacPherson G. J., and Huss G. R. (2005) Petrogenesis of Al-rich chondrules: evidence from bulk compositions and phase equilibria. *Geochim. Cosmochim. Acta* **69**, 3099–3127.

McSween H. Y. (1977) Chemical and petrographic constraints on the origin of chondrules and inclusions in carbonaceous chondrites. *Geochim. Cosmochim. Acta.* **41**, 1843–1860.

Radomsky P. M., and Hewins R. H. (1990) Formation conditions of pyroxene-olivine and magnesian olivine chondrules. *Geochim. Cosmochim. Acta* **54**, 3537–3558.

Russell S. S., Srinivasan G., Huss G. R., Wasserburg G. J., and MacPherson G. J. (1996) Evidence for widespread ^{26}Al in the solar nebula and new constraints for nebula timescales. *Science* **273**, 757–762.

Russell S. S., Huss G. R., MacPherson G. J., and Wasserburg G. J. (1997) Early and late chondrule formation: new constraints for nebula chronology from ^{26}Al/^{27}Al in unequilibrated ordinary chondrites. *Lunar Planet. Sci.* **XXVIII**, 1209–1210.

Russell S. S., MacPherson G. J., Leshin L. A., and McKeegan K. D. (2000) ^{16}O enrichments in aluminum-rich chondrules from ordinary chondrites. *Earth Planet. Sci. Lett.* **184**, 57–74.

Sheng Y. J. (1992) Origin of plagioclase-olivine inclusions. Ph. D. Thesis. California Institute of Technology.

Sheng Y. J., Hutcheon I. D., and Wasserburg G. J. (1991) Origin of plagioclase-olivine inclusions in carbonaceous chondrites. *Geochim. Cosmochim. Acta* **55**, 581–599.

Srinivasan G., Krot A. N., and Ulyanov A. (2000) Al-Mg systematics in anorthite-rich chondrules and calcium-aluminum rich inclusions from the reduced CV chondrite Efremovka. *Meteorit. Planet. Sci.* **35**, A151–A152 (abstract).

Stolper E. (1982) Crystallization sequences of Ca-Al-rich inclusions from Allende: an experimental study. *Geochim. Cosmochim. Acta* **46**, 2159–2180.

Stolper E., and Paque J. M. (1986) Crystallization sequences of Ca-Al-rich inclusions from Allende: the effects of cooling rate and maximum temperature. *Geochim. Cosmochim. Acta* **50**, 1785–1806.

Tsuchiyama A., Nagahara H., and Kushiro I. (1980) Experimental reproduction of textures of chondrules. *Earth Planet. Sci. Lett.* **48**, 155–165.

Tsuchiyama A., Osada Y., Nakano T., and Uesugi K. (2004) Experimental reproduction of classic barred olivine chondrules: open-system behavior of chondrule formation. *Geochim. Cosmochim. Acta* **68**, 653–672.

Wark D. A. (1987) Plagioclase-rich inclusions in carbonaceous chondrite meteorites: liquid condensates? *Geochim. Cosmochim. Acta.* **51**, 221–242.

Weinbruch S., Müller W. F., and Hewins R. H. (2001) A transmission electron microscope study of exsolution and coarsening in iron-bearing pyroxene from synthetic analogues of chondrules. *Meteorit. Planet. Sci.* **36**, 1237–1248.

Associate editor: Sara S. Russel